https://doi.org/10.1038/s41563-021-00981-



Enhanced substrate stress relaxation promotes filopodia-mediated cell migration

Kolade Adebowale 1,2, Ze Gong 3, Jay C. Hou4, Katrina M. Wisdom 5,6, Damien Garbett Hong-pyo Lee6, Sungmin Nam 6,8,9, Tobias Mever^{7,10}, David J. Odde 4, Vivek B. Shenov 5,5 and Oviiit Chaudhuri 5,6 × 100 ×

Cell migration on two-dimensional substrates is typically characterized by lamellipodia at the leading edge, mature focal adhesions and spread morphologies. These observations result from adherent cell migration studies on stiff, elastic substrates, because most cells do not migrate on soft, elastic substrates. However, many biological tissues are soft and viscoelastic, exhibiting stress relaxation over time in response to a deformation. Here, we have systematically investigated the impact of substrate stress relaxation on cell migration on soft substrates. We observed that cells migrate minimally on substrates with an elastic modulus of 2 kPa that are elastic or exhibit slow stress relaxation, but migrate robustly on 2-kPa substrates that exhibit fast stress relaxation. Strikingly, migrating cells were not spread out and did not extend lamellipodial protrusions, but were instead rounded, with filopodia protrusions extending at the leading edge, and exhibited small nascent adhesions. Computational models of cell migration based on a motor-clutch framework predict the observed impact of substrate stress relaxation on cell migration and filopodia dynamics. Our findings establish substrate stress relaxation as a key requirement for robust cell migration on soft substrates and uncover a mode of two-dimensional cell migration marked by round morphologies, filopodia protrusions and weak adhesions.

ell migration plays a key part in development, homeostasis, immune cell trafficking, wound healing and cancer metastasis¹. Cell migration is often studied on two-dimensional (2D) substrates where adherent cell migration is characterized by lamellipodial protrusion at the leading edge and is mediated by Rac, a growing dendritic actin network, highly spread morphologies, focal adhesions, high traction strains and myosin contractility at the trailing edge¹⁻³. Only when adherent cells are confined, as for cells migrating through dense three-dimensional (3D) matrices, microchannels or micrometre-scale spacings between flat substrates, has it been found that cells can migrate adopting rounded morphologies³⁻⁷. This contrasts the behaviour of immune cells, such as neutrophils or dendritic cells, which can migrate with rounded morphologies and weak adhesions at much higher speeds⁸⁻¹⁰. Although there are various modes of migration found under confinement, on 2D substrates, lamellipodia-mediated migration has been found to be almost universal for adherent cells. However, there is growing recognition that filopodia, thin actin-rich protrusions, couple with lamellipodia to play a key role in cell migration in certain contexts^{11,12}. Filopodia have been implicated in substrate tethering, mechanosensing and the generation of guidance cues^{11–13}.

Studies over the past four decades have elucidated molecular details of cell migration on 2D substrates and found that biophysical cues, including cell adhesion ligand density and stiffness of cell culture substrates, regulate cell migration^{2,14}. Cell migration speed peaks at intermediate ligand density and is impaired if ligand density is too low or too high^{2,15}. Further, cells exhibit increased migration speeds with increased stiffness, or display a biphasic response with respect to stiffness, with maximum migration speeds occurring at intermediate stiffnesses^{16,17}. Mirroring the finding of how stiffness impacts cell migration are findings on how substrate stiffness impacts lamellipodial and filopodial protrusions. Recent studies showed that the stability of lamellipodia protrusions increases with stiffness¹⁸. Furthermore, although the number of filopodia protrusions extending from a cell has been found to decrease with increase in stiffness, the number of stable filopodia increase with stiffness^{13,19,20}. The motor-clutch model was proposed as a framework to describe how the cell's intrinsic and extrinsic mechanical cues modulate key aspects of cell migration, adhesion dynamics and force transmission to the substrate. The stochastic model of the motor-clutch hypothesis developed by Chan and Odde mathematically describes the experimentally observed response of cell migration to substrate stiffness^{17,21}. Typically, these and other 2D migration studies explored cell migration on glass surfaces or on elastic substrates with elastic moduli in the range of tens of kilopascals^{17,22}, as cells on softer, elastic substrates are rounded and are unable to migrate robustly¹⁶.

Although stiff, elastic substrates are commonly used to study cell migration, many biological tissues are soft, with elastic moduli closer to 1 kPa23, and are viscoelastic, exhibiting stress relaxation over time in response to a deformation²⁴. Stiffness relates to the initial resistance of a material to deformation, whereas stress relaxation describes how that resistance relaxes over time. Soft biological tissues exhibit stress relaxation half times ranging from ~10 to 1,000 s^{24,25}. Recent studies have indicated substrate viscoelasticity to be a mediator of diverse cellular behaviours, including cell

Department of Chemical Engineering, Stanford University, Stanford, CA, USA. Chemistry, Engineering, and Medicine for Human Health (ChEM-H), Stanford University, Stanford, CA, USA. 3Department of Materials Science and Engineering, University of Pennsylvania, Philadelphia, PA, USA. 4Department of Biomedical Engineering, University of Minnesota, Minneapolis, MN, USA. 5 Department of Bioengineering, University of Pennsylvania, Philadelphia, PA, USA. 6Department of Mechanical Engineering, Stanford University, Stanford, CA, USA. 7Department of Chemical and Systems Biology, Stanford University School of Medicine, Stanford, CA, USA. 8 John A. Paulson School of Engineering and Applied Sciences, Harvard University, Cambridge, MA, USA. 9 Wyss Institute for Biologically Inspired Engineering, Harvard University, Boston, MA, USA. ¹⁰Department of Cell and Developmental Biology, Weill Cornell Medical College, New York, NY, USA. [™]e-mail: chaudhuri@stanford.edu

spreading²⁶⁻²⁹, stem cell differentiation^{24,30}, cell proliferation^{30,31} and cartilage matrix formation³². Substrate stress relaxation also impacts the type and extent of substrate adhesions formed, with the relation dependent on cell and substrate type^{26,27,29,30}. However, the impact of substrate stress relaxation on cell migration, lamellipodial protrusions and filopodia remains unclear. Here, we report the results of a systematic investigation of the role of substrate stress relaxation on cell migration on soft, viscoelastic substrates. We show that faster substrate stress relaxation enhances cell migration and increases filopodia length and lifetime. Further, we demonstrate that cells use a mode of migration, mediated by filopodia but not lamellipodia, to migrate on soft, viscoelastic substrates.

Results

Faster substrate stress relaxation enhances cell migration. We used viscoelastic substrates with independently tunable stress relaxation for 2D cell migration studies. These substrates consist of interpenetrating networks (IPNs) of alginate and reconstituted basement membrane (rBM) matrix^{4,28}. Alginate, an inert block copolymer, displays limited susceptibility to degradation by proteolysis by mammalian enzymes, and is crosslinked into a network with calcium. The rBM matrix contains cell adhesion ligands relevant to the basement membrane, and was chosen because cancer cells migrating in vivo and in vitro have been shown to migrate along and interact with basement membrane-rich interfaces^{33,34}. By varying the amount of ionic calcium crosslinker and the molecular weight of the alginate^{4,24,28}, the mechanical properties of the IPNs were varied to obtain IPNs with a range of stress relaxation behaviours but similar initial elastic moduli of ~2 kPa (Fig. 1a,b and Supplementary Fig. 1). This enabled an unambiguous attribution of any differences observed in cell migration to differences in stress relaxation, not stiffness or cell adhesion ligand density. Additionally, polyacrylamide (PA) gels coated with rBM were used as model elastic substrates for comparison³⁵. The stress relaxation for the IPNs is quantified by the time it takes for the normalized stress to reduce to one-half its peak value $(t_{1/2})$. The $t_{1/2}$ values were ~100, ~240 and ~2,200 s for the IPNs, which were termed fast-relaxing, medium-relaxing and slow-relaxing, respectively, based on the relation of these relaxation times to those in soft tissues (Fig. 1c). The elastic PA gels exhibited negligible stress relaxation (Fig. 1c). Note that although these viscoelastic IPNs also exhibited mechanical plasticity⁴, hydrogel deformation was mostly reversible and elastic over timescales relevant to cell migration on the 2D substrates.

We investigated the impact of substrate stress relaxation on cell migration. Live-cell confocal microscopy was used to follow the migration of human HT-1080 fibrosarcoma cells, MDA-MB-231 breast cancer cells and MCF-10A mammary epithelial cells—cell lines widely used in cell migration studies—on fast-, medium- and slow-relaxing IPNs as well as elastic PA gels and glass substrates. Sample migrating cells and migration tracks show that faster stress relaxation enhances cell migration (Fig. 1d and Supplementary Videos 1 and 2). Quantification of the mean squared displacement (MSD) and speed for HT-1080 cells indicates that cells migrate further and faster on fast- and medium-relaxing substrates compared with on slow-relaxing substrates (Fig. 1e,f). For example, over 1h, HT-1080 cells migrate ten times further on fast-relaxing substrates than on slow-relaxing substrates. For comparison, HT-1080 cells migrate minimally on elastic PA substrates with a modulus of 2 kPa, but with much higher speeds and distances on substrates with a modulus of ~40 kPa and glass (Fig. 1g,h). Although cells migrate to a slightly greater extent on 2-kPa elastic substrates than on 2-kPa substrates that are slow-relaxing, ligand presentation and density likely differ between IPNs and PA gels. Intracellular calcium imaging indicates that these differences are not due to the different calcium amounts used in hydrogel formulation (Supplementary

Fig. 2 and Supplementary Table 1). As with the HT-1080 cells, the MDA-MB-231 and MCF-10A cells moved farther and faster on fast-relaxing IPNs than on slow-relaxing IPNs (Fig. 1i-l). Together, these data show that faster stress relaxation enhances cell migration on soft substrates.

Lamellipodia-independent migration on fast-relaxing substrates. Next, we investigated whether the migration mode observed on soft-

and fast-relaxing substrates matched the canonical lamellipodiamediated migration mode previously described on glass and stiff elastic substrates. As such, we first examined the cell morphology, because 2D cell migration on glass or stiff elastic substrates is tightly linked to spread morphologies. HT-1080 cells were much more rounded, with greater circularity and less spread on fastand slow-relaxing IPNs. The observed cortical actin structure was markedly different from the actin-rich stress fibres and dense meshwork of actin at the leading edge observed in cells on glass substrates (Fig. 2a). Further, the fan-shaped architecture observed on glass, characteristic of lamellipodia, was absent on viscoelastic substrates (Fig. 2a,b). Quantification of the circularity and 2D cell spread area shows strong differences in these parameters between cells on viscoelastic substrates and cells on elastic substrates (Fig. 2c-e). One possible explanation for these differences could be that cells on fast-relaxing IPNs are generally less spread but become more spread only when they migrate. However, analysis of instantaneous speed and circularity indicated that migrating cells on viscoelastic substrates are more circular than migrating cells on elastic substrates, and lamellipodia were observed on spread cells on glass substrate (Supplementary Fig. 3). To summarize, these data indicate that cells use rounded morphologies to migrate on soft, viscoelastic substrates without the use of lamellipodia, which adherent cells almost always use to migrate on glass or stiff and elastic substrates.

Migration mediated by filopodia protrusions. As morphological analysis suggested a lamellipodia-independent mode of migration, we sought to determine what other cellular processes might mediate migration on soft, viscoelastic substrates. Cells migrating on fast-relaxing IPNs frequently displayed long, thin, protrusions, reminiscent of filopodia, whereas lamellipodia were observed on glass (Fig. 3a,b). Cells on substrates with slow relaxation occasionally extended individual protrusions, whereas cells on fast-relaxing IPNs extended an average of six protrusions every 10 min (Fig. 3c). Importantly, pharmacological inhibition of fascin and formin, two key proteins involved in filopodia formation^{20,21}, diminishes the number of protrusions, suggesting these protrusions to be filopodia (Fig. 3d)12,13. Immunofluorescence staining revealed the characteristic localization of myosin-X and vasodilator stimulated phosphoprotein (VASP) at the tip of long actin-rich protrusions (Fig. 3e,f), features unique to filopodia^{13,36}, further supporting the notion that the protrusions are filopodia. Faster substrate stress relaxation increases the number of myosin-X puncta observed at the cell periphery, some of which are associated with actin protrusions (Fig. 3g). Not only are these protrusions lost upon inhibition of fascin and formin, but migration is also reduced, indicating that filopodia protrusions are important for cell migration (Fig. 3d,h). In addition, short interfering RNA (siRNA) knockdowns of fascin1 and myosin-X substantially diminished cell migration, further confirming the role of filopodia in cell migration (Fig. 3i,j). Taken together, these results demonstrate the role of filopodia in mediating cell migration on soft, viscoelastic substrates.

Migration mediated by nascent adhesions. Next, we sought to elucidate the impact of substrate stress relaxation on cell-substrate adhesions and force generation, as these typically underlie adherent cell migration on 2D substrates. Paxillin, a universal component of

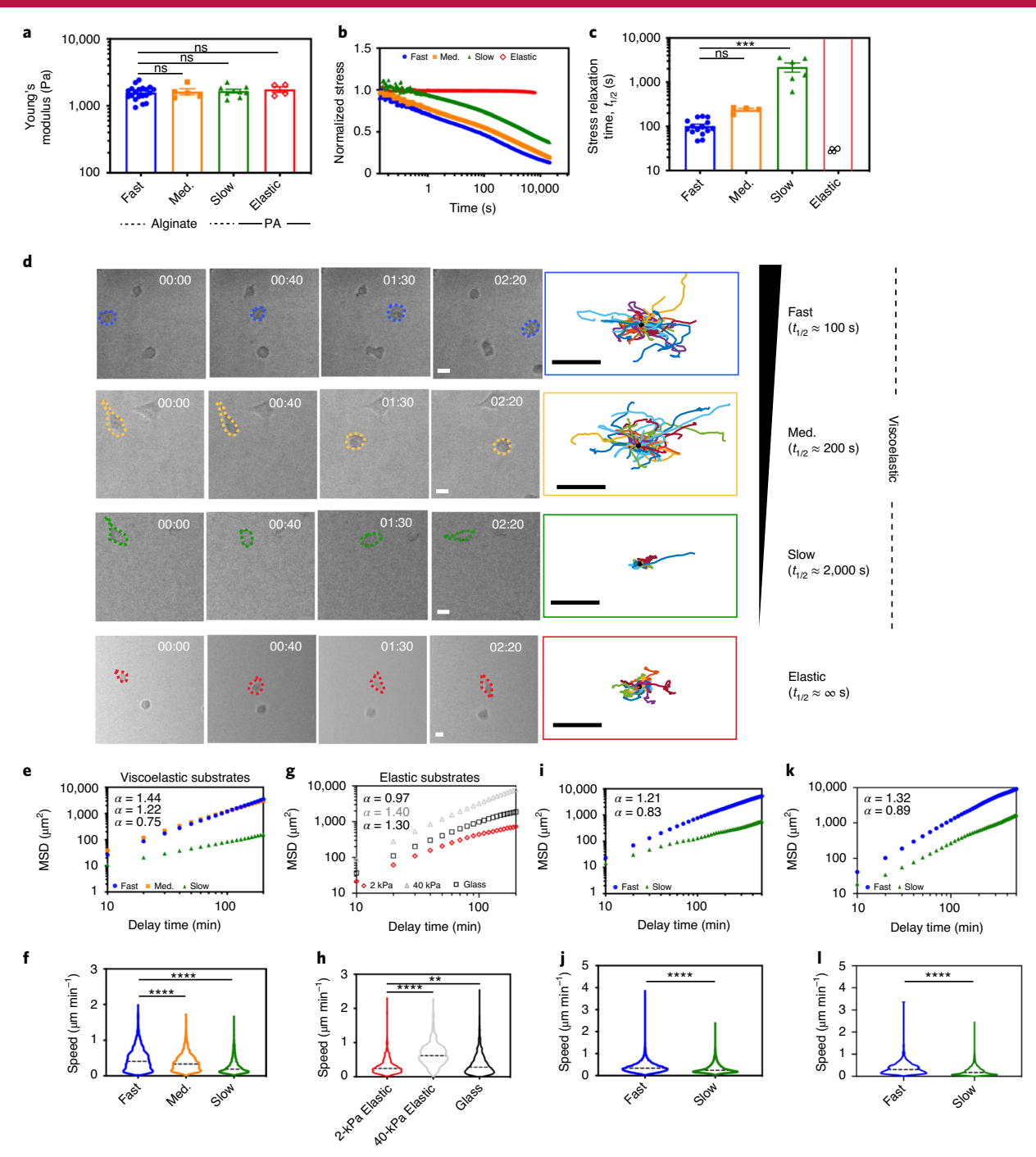


Fig. 1| Substrate stress relaxation regulates cell migration on soft substrates. a, Young's modulus of three different formulations of alginate-rBM IPNs (fast, medium (med.) and slow) and a PA gel. Kruskal-Wallis with Dunn's multiple comparisons test was used for analysis of the data, comparing with the fast-relaxing hydrogel: not statistically significant, ns P > 0.9999; n = 20, 5, 9 and 4 independent samples (fast, med., slow and elastic). **b**, Representative stress relaxation tests on the different IPNs. \mathbf{c} , Time for the normalized stress in the IPNs to reduce to one-half $(t_{1/2})$ the original value in stress relaxation tests. Kruskal-Wallis with Dunn's multiple comparisons test was used for analysis of the data, comparing with the fast-relaxing hydrogel: ns P = 0.0653, ***P = 0.0001; n = 15, 4, 6 and 4 independent samples (fast, med., slow and elastic). The elastic gel does not show any stress relaxation. The data in **a** and **c** are presented as mean values ± s.e.m. **d**, Time series of images of HT-1080 cells on the indicated IPNs. The far-right panels show the trajectories of ~80 randomly selected migrating cells for each condition. Times are indicated in h:min. Scale bars, 20 µm (cells) and 100 µm (trajectories). e-I, The mean squared displacement (MSD) versus time lag between positions, delay time (e,g,i,k) and cell migration speeds (f,h,j,l) for HT-1080 (e-h), MDA-MB-231 (i,j) and MCF-10A (k,l) human cancer cell lines cultured on viscoelastic or elastic substrates. In e,g,i and k, MSD ∝ t^a. In f, Kruskal-Wallis with Dunn's multiple comparisons test was used for analysis of the data, comparing with the fast-relaxing hydrogel: ****P < 0.0001; n = 2,309, 1,263 and 1,809 (fast, med. and slow) cells examined over three independent samples. In h, Kruskal-Wallis with Dunn's multiple comparisons test was used for analysis of the data, comparing with the 2-kPa elastic: **P=0.0086, ****P < 0.0001; n=471, 611 and 3,651 (fast, med. and slow) cells examined over two independent samples. In \mathbf{j} , the Kolmogorov-Smirnov test was used for data analysis: ****P < 0.0001; n = 4,651 and 4,501 (fast and slow) cells examined over two independent samples. In I, the Kolmogorov-Smirnov test was used for data analysis: ****P<0.0001; n=1,561 and 1,115 (fast and slow) cells examined over two independent samples. The dashed lines in the violin plots represent median values. All statistical tests were two-sided.

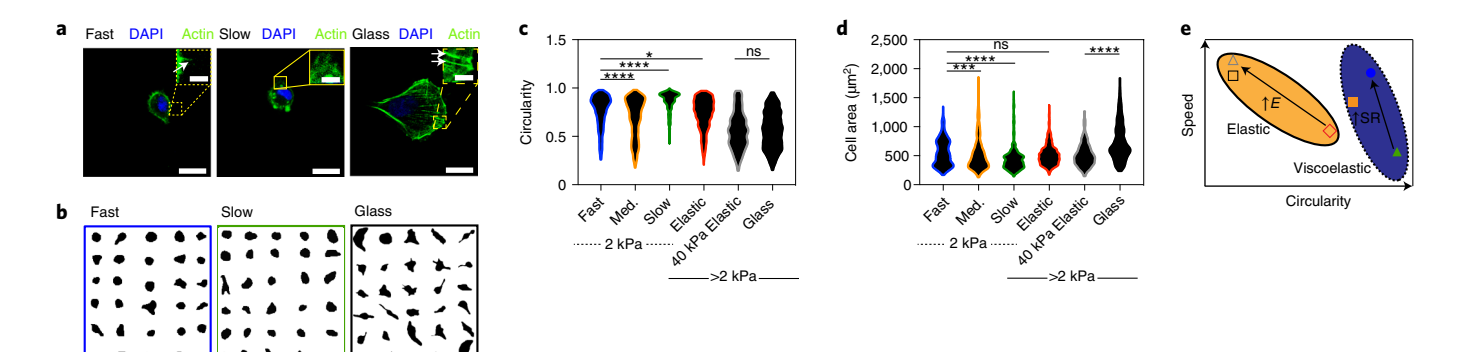


Fig. 2 | Cells migrate on viscoelastic substrates with rounded morphologies. a, HT-1080 cells on fast-relaxing, slow-relaxing and glass substrates. Actin is highlighted in green and the nuclei (DAPI, 4,6-diamidino-2-phenylindole) in blue. Scale bars, 20 μm; inset scale bars, 5 μm. **b**, Cell outlines of randomly selected HT-1080 cells on fast-relaxing, slow-relaxing and glass substrates. Scale bars, 20 μm. **c**, Circularity of HT-1080 cells on viscoelastic (fast-, medium- and slow-relaxing) and elastic (2-kPa PA, 40-kPa PA and glass) substrates. Kruskal-Wallis with Dunn's multiple comparisons test was used for analysis of the data, comparing with the fast-relaxing hydrogel: ns P > 0.9999, P = 0.0131, ****P < 0.0001; n = 630, 1,119, 630 and 715 (fast, med., slow and glass) cells over three independent samples, and n = 788 and 376 (elastic and 40-kPa elastic) cells examined over one independent sample. **d**, Spreading areas of HT-1080 cells on viscoelastic (fast-, medium- and slow-relaxing) and elastic (elastic, 40-kPa elastic and glass) substrates. Kruskal-Wallis with Dunn's multiple comparisons test was used for analysis of the data, comparing with the fast-relaxing hydrogel: ns P > 0.9999, ***P = 0.0002, ****P < 0.0001; n = 630, 1,119, 630 and 715 cells (fast, med., slow and glass) over three independent samples, and n = 788 and 376 cells (elastic and 40-kPa elastic) examined over one independent sample. The dashed lines in the violin plots represent median values. All statistical tests were two-sided. **e**, Schematic showing instantaneous speed versus circularity for HT-1080 cells on viscoelastic substrates (purple oval with dotted boundary) and elastic substrates (tan oval with solid boundary). Filled blue circle, fast-relaxing gel; filled orange square, medium-relaxing gel; filled green triangle, slow-relaxing gel; open red diamond, 2-kPa elastic gel; open silver triangle, 40-kPa elastic gel; open black square, glass. SR, stress relaxation; E, Young's modulus.

nascent and mature adhesions and essential for adhesion-dependent cell migration, was first examined³⁷. Cells on fast- and slow-relaxing substrates displayed only dot-like, peripheral, paxillin structures, indicative of nascent adhesions (Fig. 4a). Cells formed higher numbers of paxillin adhesions on fast-relaxing substrates than on slow-relaxing substrates (Fig. 4b). For comparison, cells on glass substrates displayed large and elongated paxillin structures, reminiscent of mature focal adhesions, in addition to nascent adhesions, with around ten times more paxillin adhesions compared with cells on fast-relaxing substrates (Fig. 4a,b). These analyses indicate that fewer, weak, paxillin adhesions are associated with cell migration on fast-relaxing substrates. As adhesions connect actomyosin-based contraction to substrates for force generation, we investigated actin and myosin structures on fast-relaxing substrates. Actin is localized at the cell periphery, and substantially fewer phosphorylated myosin rich puncta are observed, mostly localized proximal to the cell membrane, on fast-relaxing substrates than on glass substrates

In addition, we elucidated the nature of traction stresses associated with cell migration on fast-relaxing substrates. Fluorescent beads were embedded into the gels to monitor traction strains associated with migration. An upper bound on traction stresses can be estimated by assuming the substrates to be elastic and converting traction strains into stresses as in traction force microscopy. As would be anticipated by the fewer adhesions on slow-relaxing substrates than on fast-relaxing substrates, the upper bound on traction stresses are correspondingly lower on the slow-relaxing substrates (Fig. 4d). An upper bound on maximum traction stresses on viscoelastic substrates is estimated to be ~100 Pa, which is comparable to the median value for maximum traction stresses observed on elastic substrates (Fig. 4e). Cell migration on fast-relaxing IPNs is saltatory, with cell translocation punctuated by periods in which the cell deforms the substrate (Fig. 4f). During translocation, cells push on the substrate, and the highest substrate displacement is observed at the leading edge of translocating cells. Following translocation, the beads return to their initial positions, indicating that substrate deformations during migration are elastic and that substrate remodelling is negligible (Supplementary Video 3). Together, these results indicate that migration on soft, fast-relaxing IPNs requires nascent adhesions and contractility, and is associated with protrusive deformations at the leading edge.

Further, we investigated the role of integrins, actin network activity and actomyosin-based contractility in cell migration on fast-relaxing substrates. First, $\beta 1$ -integrin inhibition and overactivation, using blocking or activating antibodies, substantially diminished cell migration speeds (Fig. 4g), suggesting that integrin engagement is important for cell migration. Next, modulation of actin network activity by inhibiting actin polymerization with latrunculin A, restricting the nucleation of growing actin filaments as branches by inhibiting the Arp2/3 complex or inhibiting Rac1, a Rho GTPase that orchestrates actin network growth, led to reduction in cell motility (Fig. 4h). Further, inhibition of myosin activity diminished cell motility (Fig. 4i). These perturbation studies confirm the role of integrin-based adhesions, actin polymerization and actomyosin contractility in mediating cell migration on fast-relaxing substrates.

Motor-clutch models reproduce the experimentally observed impact of stress relaxation. Next, we investigated whether the motor-clutch model could explain the experimental results using two motor-clutch based simulations. First, a 2D cell migration simulator (CMS) was implemented to investigate the cell migration differences between fast- and slow-relaxing viscoelastic substrates, and between different stiffness values for elastic substrates (Fig. 5a and the Supplementary Information). The CMS is composed of multiple modules to represent cell protrusions, and each module is described by the motor-clutch model^{21,38}. The CMS incorporates mass conservation for actin, myosin and clutches, as well as allowing actin filaments to spontaneously form and grow in length. This model predicts that cell migration speed reaches a maximum value at an optimal stiffness on purely elastic substrates¹⁷. In the current work, the CMS was used to simulate viscoelastic substrates using a standard linear viscoelastic solid (SLS) model with fixed initial and long-term moduli. The number of motors and clutches were

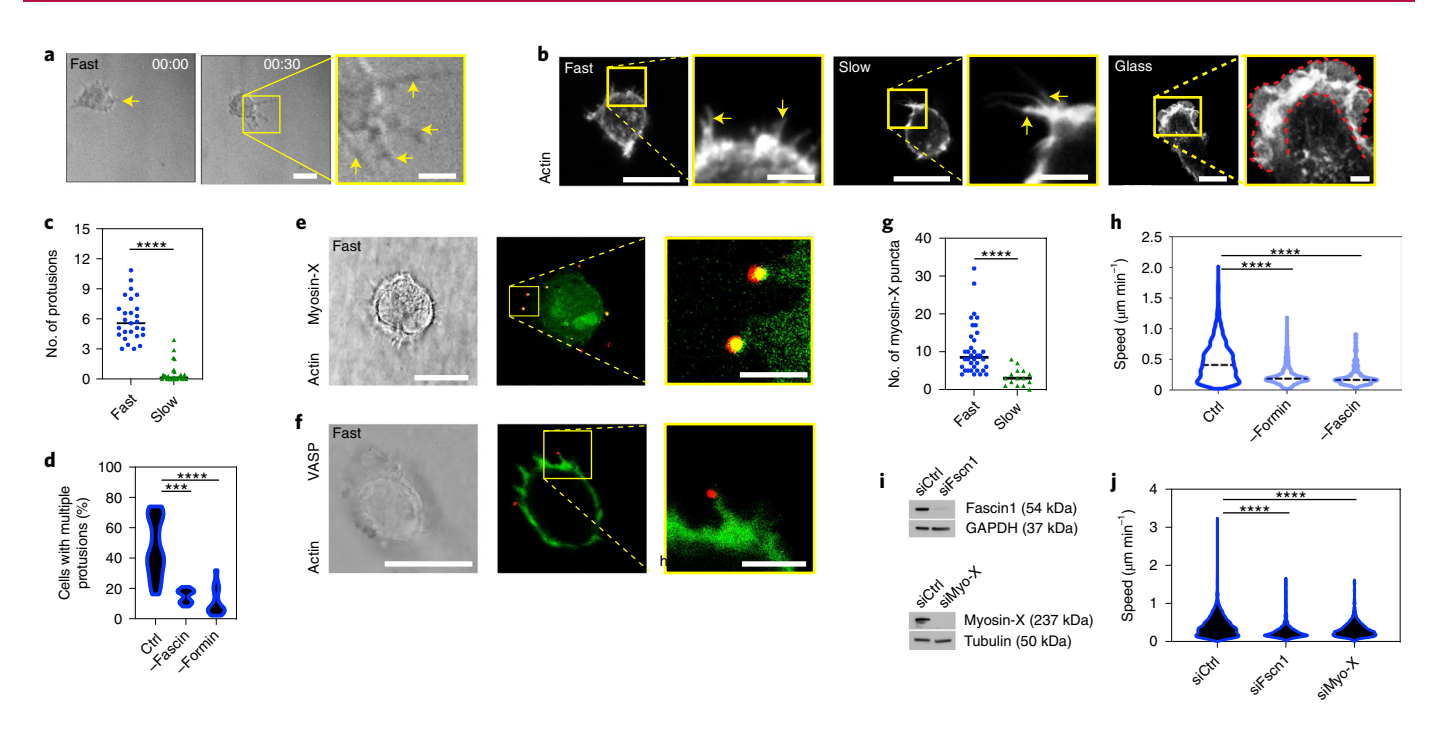


Fig. 3 | Filopodia protrusions mediate migration on soft, fast-relaxing substrates. a, A migrating HT-1080 cell displays multiple protrusions (yellow arrows) at the leading edge. The left image has the same scale bar as the middle image. Times are indicated in h:min. b, The HT-1080 cell displays filopodia protrusions (yellow arrows) on fast- and slow-relaxing substrates. Lamellipodia (red outline) are observed on the spread cell on glass. c, The number of protrusions from HT-1080 cells on fast- and slow-relaxing viscoelastic substrates. The Kolmogorov-Smirnov test was used for data analysis: ****P<0.0001; n=27 cells each examined over two independent samples. d, The percentage of HT-1080 cells with protrusions without inhibitor (Ctrl, control) and with inhibition of fascin (30 μM fascin-G2) and formin (20 μM SMIFH2). Kruskal-Wallis with Dunn's multiple comparisons test was used for analysis of the data: ***P = 0.0003, ****P < 0.0001; n = 22, 11 and 13 (Ctrl, -fascin and -formin) cells examined over three independent samples (two for fascin). e.f. Actin with myosin-X (e) or VASP (f) staining for HT-1080 cells on fast-relaxing substrates. For a,b,e and f: scale bars, 20 μm; zoom-in/inset scale bars, 5 μm. The middle images in e and f have the same scale bar as the left images. g, The number of peripheral puncta of myosin-X in HT-1080 cells on fast- and slow-relaxing substrates. The Kolmogorov-Smirnov test was used for data analysis: ****P < 0.0001; n = 36 and 15 (fast and slow) cells examined over two independent samples. h, HT-1080 cell migration speed without inhibitor and after inhibition of fascin (30 μM fascin-G2) and formin (20 μM SMIFH2). Kruskal-Wallis with Dunn's multiple comparisons test was used for analysis of the data: ****P < 0.0001; n = 2,309, 1,302 and 171 (Ctrl, -formin and -fascin) cells examined over three, two and one independent samples, respectively. i, Western blot for siRNA knockdown of fascin1 and myosin-X. siCtrl, siRNA empty control; siFscn1, siRNA of fascin1; siMyo-X, siRNA of myosin-X. Glyceraldehyde 3-phosphate dehydrogenase (GAPDH) and tubulin are the respective loading controls. j, HT-1080 cell migration speed with knockdown of fascin1 and myosin-X. Kruskal-Wallis with Dunn's multiple comparisons test was used for analysis of the data: ****P < 0.0001; n = 1,892, 937 and 1,237 (siCtrl, siFSCN1 and siMYO-X) cells examined over two independent samples. All the data presented in d,h and j are for cells on fast-relaxing substrates. The dashed lines in the violin plots represent median values. The solid lines in the scatter plots indicate median values. Comparisons were made to fast-relaxing hydrogel without perturbation. All statistical tests were two-sided.

adjusted for the elastic and viscoelastic substrates because the maximum traction stresses are higher on elastic substrates. The migration speed deriving from the CMS was found to increase with faster substrate stress relaxation and increased stiffness. These trends are in agreement with experimental findings (Fig. 5b,c). In addition, the simulation results are in agreement with the observed impact of stress relaxation on cell morphology and cell area (Supplementary Fig. 4). Furthermore, the CMS results show that cell migration is reduced upon inhibition of adhesion, actin polymerization and myosin activity, all consistent with experimental findings (Fig. 5d–f). To summarize, the CMS results show close agreement with the observed experimental trends for migration speed as a function of stress relaxation on viscoelastic substrates and stiffness on elastic substrates, as well as the impact of inhibition of adhesion, actin polymerization and actomyosin contraction.

Next, we applied a distinct one-dimensional (1D) motor-clutch-based model to obtain mechanistic insight into the impact of varying levels of substrate stress relaxation on cell migration²⁷. A consequence of stress relaxation is a decrease of the initial moduli to a lower long-term moduli. The relaxation timescale parameter in the SLS model was varied, while fixing the initial and long-term

moduli, in 1D Monte Carlo simulations of migration (Fig. 5g). As a first step, we validated that the simulation replicated key experimental findings. Simulations predicted that faster relaxation increases migration distance and MSD, and that the MSDs follow a powerlaw relation with time, all matching the experimental findings (Fig. 5h,i). These simulations reveal insights into the molecular mechanisms by which substrate viscoelasticity impacts cell migration. Initially, opposite ends of the cell share the same number of bound clutches (Fig. 5j,k and Supplementary Fig. 5). However, the stochastic bond (clutch) dynamics cause an asymmetry in the bound clutch number between the left and right ends. At the end with less bound clutches (left end in Fig. 5j), each bond now transmits higher tensile force, and hence has a higher probability of breaking due to the force-dependent unbinding of the clutches. As each bond breaks, even more force is carried by each clutch. Subsequently, the entire stretch of adhesions on this side breaks catastrophically, leading to an increased retrograde flow velocity (Fig. 5j). The unbound end retracts quickly, leading to cell migration towards the right end. Interestingly, this sequence of events is consistent with the experimental traction strain measurements, as translocation of the cell to the right end is accompanied by a release of tractions on the left end

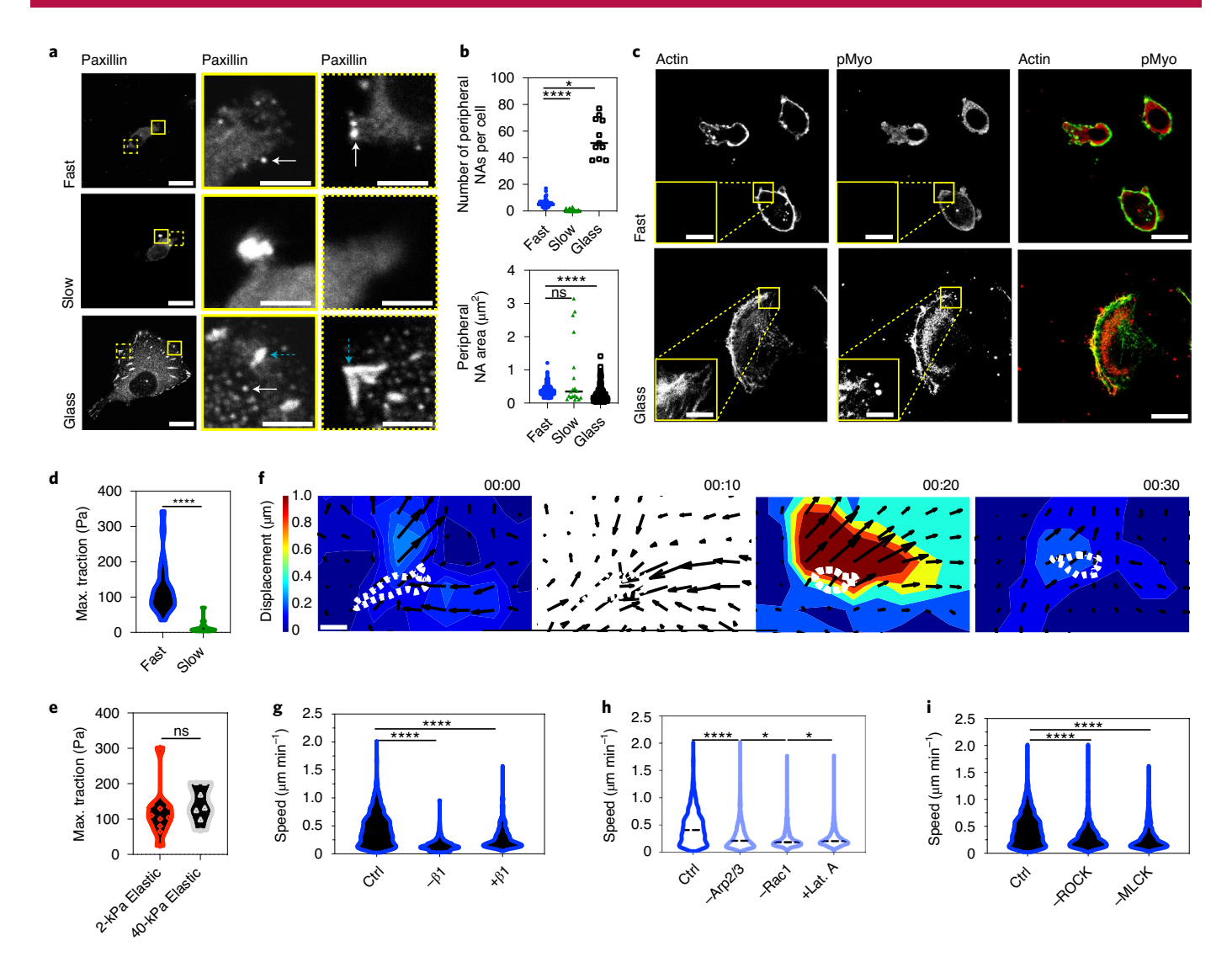


Fig. 4 | Adhesion and traction force mediate migration on fast-relaxing substrates. a, Immunofluorescence of paxillin on fast- and slow-relaxing substrates as well as on glass. b, Number of peripheral paxillin adhesions (PAs) (top) and area of nascent adhesions (NAs) (bottom) on fast- and slow-relaxing substrates and on glass. Kruskal-Wallis with Dunn's multiple comparisons test was used for analysis of the data: ns P = 0.6074, *P = 0.0115, ****P < 0.0001. For the puncta number, the data are averages of n = 57, 60 and 11 (fast, slow and glass) cells. For the area, the data are averages of n = 346, 19 and 644 (fast, slow and glass) adhesions. Samples were examined over one independent sample. The solid lines in the scatter plots indicate median values. c, Immunofluorescence staining of actin and phosphorylated myosin (pMyo) on fast-relaxing and glass substrates. d,e, Maximum traction stress during migration on viscoelastic (\mathbf{d}) and elastic (\mathbf{e}) gels. The Kolmogorov-Smirnov test was used for data analysis: ns P = 0.5943; ****P < 0.0001; n = 20, 20, 10 and 7 (fast, slow, 2-kPa elastic and 40-kPa elastic) cells each over one independent sample. f, Representative substrate displacement for a migrating (left to right) HT-1080 cell (white outline). The arrows indicate direction of substrate displacement. Times are indicated in h:min. For a.c and f: scale bars, 20 µm; zoom-in/inset scale bars, 5 µm, g. HT-1080 cell migration speed on the fast-relaxing substrate with (-\textit{-}\textit{B1}) and without (Ctrl) addition of $5 \mu g m l^{-1} \beta 1$ -integrin blocking or with $2 \mu g m l^{-1} TS2/16$ activating antibodies (+ $\beta 1$). The Kolmogorov-Smirnov test was used for data analysis: ****P < 0.0001; n = 2,309,430 and 825 (Ctrl, $-\beta 1$ and $+\beta 1$) cells examined over two independent samples for $-\beta 1$ and $+\beta 1$, and three for Ctrl. **h**, HT-1080 cell migration speed on fast-relaxing substrate with and without inhibition of actin polymerization with latrunculin A (Lat. A, 100 nM), Rac1 (70 µM NSC 23766) and Arp2/3 (50 μM CK 666). Kruskal-Wallis with Dunn's multiple comparisons test was used for analysis of the data: *P = 0.0133 and 0.0148, ****P < 0.0001; n=2,309, 1,913, 1,233 and 1,996 (Ctrl, -Arp2/3, -Rac1 and +Lat. A) cells examined over three independent experiments for Ctrl, -Rac1 and +Lat. A, and four for -Arp2/3. i, HT-1080 cell migration speed on fast-relaxing substrate with and without addition of ROCK inhibitor (50 μM Y-27632) and MLCK inhibitor (25 µM ML-7). The Kolmogorov-Smirnov test was used for data analysis: ****P < 0.0001; n = 2,309, 1,649 and 1,661 (Ctrl, -ROCK and -MLCK) cells examined over three independent samples for Ctrl and -MLCK, and five for -ROCK. The data in **b,d,g,h** and **i** were compared with the fast-relaxing hydrogel. The dashed lines in the violin plots represent median values. All statistical tests were two-sided.

(Fig. 5k). Additionally, the simulations predict that the cell-matrix bond lifetime should increase with faster substrate stress relaxation (Fig. 5l). Bonds experience a lower force loading rate on substrates with fast stress relaxation, leading to longer bond lifetimes prior to rupture (Fig. 5m). This prediction was tested experimentally

by introducing $\beta 1$ -integrin blocking into the media after cells had adhered to the substrates. The $\beta 1$ -blocking antibody can attach to unbound integrins, preventing these integrins from participating in further integrin–extracellular matrix (ECM) bonding. The greater the intrinsic off-rate (shorter lifetime), the higher the likelihood of

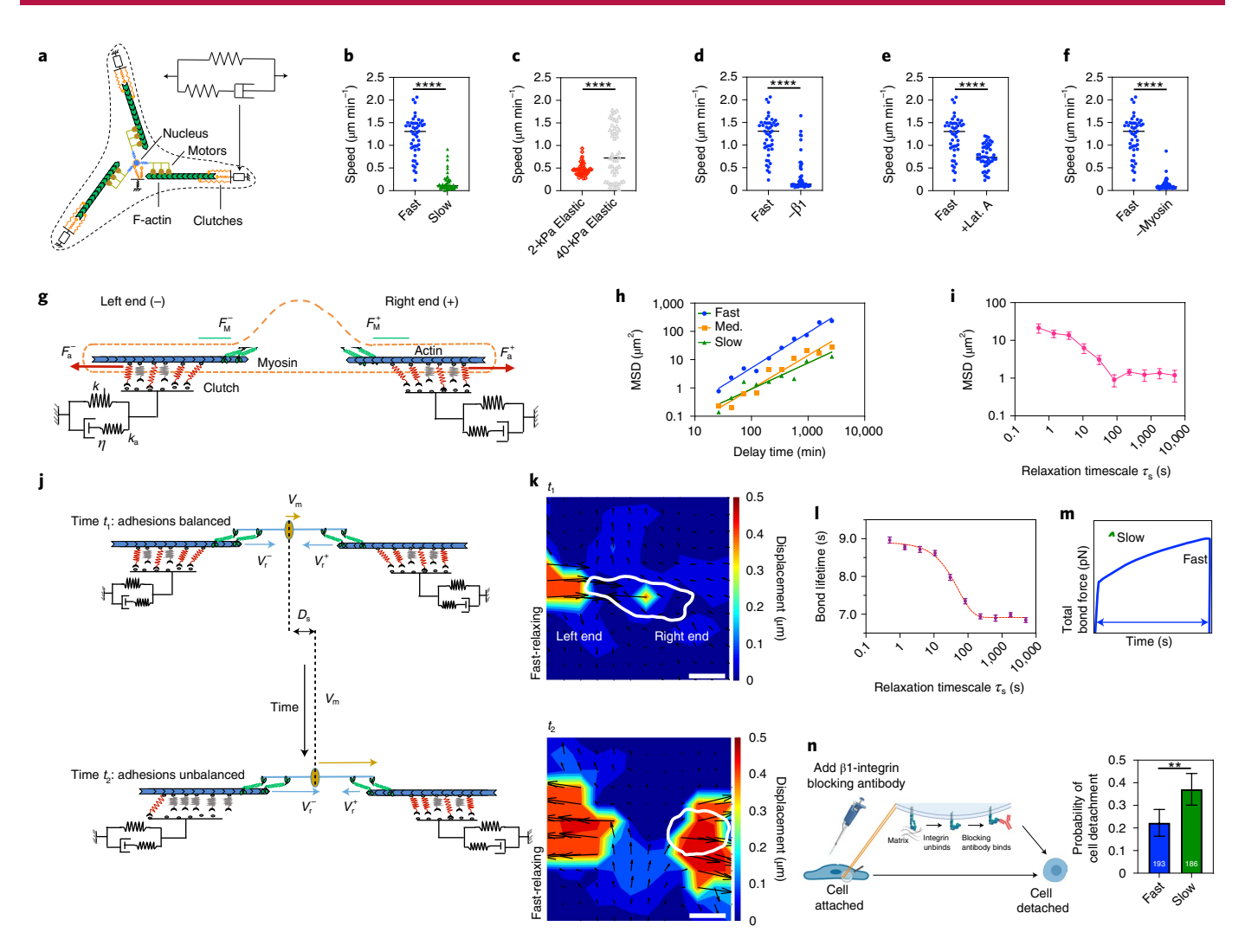


Fig. 5 | Simulations capture the impact of substrate stress relaxation on cell migration. a, Schematic of the 2D CMS used to simulate cell migration on viscoelastic substrates. b,c, Cell migration speeds on viscoelastic (b) and elastic (c) substrates predicted by the simulator. The Kolmogorov-Smirnov, two-sided, test was used for data analysis: ****P < 0.0001; n = 47, 49, 51 and 49 (fast, slow, 2-kPa elastic and 40-kPa elastic) cells over four independent simulations. **d-f**, Reducing the number of clutches n_c (- β 1) (**d**), halving the actin polymerization rate (+Lat. A) (**e**) and lowering the number of motors $n_{\rm m}$ (-myosin) (f) in the simulation leads to a decrease in the migration speed compared with the control fast-relaxing substrate. $n_{\rm r}$ = 750 and 150 (fast and $-\beta 1$), and $n_m = 1,000$ and 750 (fast and -myosin). The Kolmogorov-Smirnov, two-sided, test was used for data analysis: ****P < 0.0001; n = 47 (fast), 48 (-\beta1 and +Lat. A) and 54 (-myosin) cells over two independent simulations. The solid lines in the scatter plots indicate median values. g, Schematic of the 1D motor-clutch model of cell migration on a viscoelastic substrate. F_{M} : total maximal myosin force; F_{a} : sum of all forces sustained by bound clutches;k,: additional stiffness;k; long-term stiffness;n: dashpot viscosity. h, Simulated MSD versus time on fast-, medium- and slow-relaxing substrates. The solid lines are fits. Data from ten independent simulations. **i**, Simulated MSD as a function of relaxation timescale τ_s . The red line is a fit to the results. n=20 cells examined over 20 independent simulations. **i**, Schematic of the 1D simulation finding of balanced adhesions in the stationary cell (top) and unbalanced adhesions in the migrating cell (bottom). V_m : cell (nucleus) moving velocity; V_s : actin retrograde flow; D_s : cell displacement. \mathbf{k} , Traction strain map showing the initial strain on the cell and when the adhesions break and the cell releases the tug on the matrix. Cell migration occurs from left to right. Scale bars, 20 μ m. I, Bond lifetime τ_i (time elapsed between initial attachment of a single bond to its breakage) versus τ_s . Data are presented as mean values \pm s.e.m.; n = 20 cells examined over 20 independent simulations. **m**, Total bond force versus time for fast- and slow-relaxing substrates. n, Mean probability of cell detachment in the adhesion release experiment. The error bars indicate 95% confidence interval. Fisher's exact, two-sided, test was used for data analysis: **P=0.0017; n=193 and 186 (fast and slow) cells examined over two independent experiments. Integrin bound to the matrix stochastically unbinds, allowing the blocking antibody to bind integrin.

 β 1-integrin blocking, and consequently, the higher the probability of cell detachment. Over a 10-h window, a higher probability of cell detachment from slow-relaxing gels compared with on fast-relaxing gels was measured, indicating a higher bond lifetime for cells on the fast-relaxing gels (Fig. 5n). In summary, the observed stiffness and bond dynamics are similar to previous observations of the motor–clutch hypothesis, further implicating this hypothesis in our observations²¹.

Motor-clutch model predicts filopodia dynamics. After finding that the motor-clutch model can predict the impact of stress relaxation on cell migration, we sought to assess the validity of the model by investigating whether predictions of the model regarding filopodia dynamics were borne out by experimental observations. Filopodia protrusions were observed to be highly dynamic on both fast- and slow-relaxing substrates (Fig. 6a and Supplementary Videos 4 and 5). The 1D motor-clutch model predicted that faster

substrate stress relaxation increases both filopodia length and lifetime, as well as a correlation between both of these variables (Fig. 6b–d and Supplementary Fig. 6). All three of these predictions were validated experimentally (Fig. 6e–g). Further, the range of values obtained for filopodia length and lifetime are similar to what has been previously reported for filopodia^{20,39,40}. Overall, the experimental and simulation data demonstrate that substrate stress relaxation mediates filopodia behaviour and migration phenotype (Fig. 6h). Thus, these data indicate that substrate viscoelasticity impacts cell migration through regulation of motor–clutch dynamics and filopodia lifetimes.

Outlook

In this study we have found that substrate stress relaxation is a key modulator of adherent cell migration on soft, viscoelastic substrates. Our results demonstrate that faster substrate stress relaxation promotes increased migration distance and speed on soft substrates that are viscoelastic (Fig. 6h). These results are consistent for HT-1080 and MDA-MB-231 cells, two cancer cell lines that are broadly used for cell migration studies, as well as for non-tumorigenic MCF-10A epithelial cells. However, it is possible that some adherent cells exhibit migration phenotypes different from what we have observed here. Robustly migrating cells on fast stress-relaxing IPNs are rounded and characterized by paxillin adhesions and long, thin filopodia protrusions at the leading edge. Furthermore, faster substrate relaxation increases filopodia number, adhesions, filopodia length and lifetime, allowing filopodia to grow in length. Filopodia, in turn, regulate cell migration. These observations establish that, when presented with the appropriate biophysical cues, cells can display different migration modes beyond the canonical mode of 2D cell migration, which is characterized by high tractions, focal adhesions and lamellipodia. Taken together, our results demonstrate that substrate stress relaxation is a fundamental substrate mechanical property that regulates cell migration and filopodial protrusions.

Our study of cell migration on soft, viscoelastic substrates was motivated by the emerging recognition that many soft tissues exhibit substantial viscoelasticity^{24,41}. The viscous characteristics of biological tissues, as characterized by the loss modulus, are typically around 10% of their elastic characteristics, as characterized by the storage modulus^{26,42}. Similarly, stress relaxation tests, in which the stress is measured in response to a constant strain and where stress corresponds to the resistance to deformation, show that many biological soft tissues relax stress on timescales of a few seconds to tens of minutes⁴³. For instance, rat brain, rat liver and rat skin have been reported to have characteristic stress relaxation half times of ~1 s, ~50 s and ~650 s, respectively, whereas human breast cancer tissue has a stress relaxation half time of ~10 s (ref. 43). However, these times can vary depending on the modality of measurement and level of strain imposed⁴². Importantly, alterations in tissue viscoelasticity are associated with the progression of human pathologies like cancer and fibrosis^{4,26,44}. A recent study found that associated with the transformation of healthy pancreas to pancreatic cancer is a decrease in the characteristic decay time from ~93 to 66s (ref. 41). The results of our study indicated that such alterations in stress relaxation may impact processes involving cell migration in these contexts.

In contrast to the lamellipodia-mediated migration typically observed for cells on 2D stiff, elastic substrates, cell migration on viscoelastic substrates is lamellipodia-independent, and instead mediated by filopodia. Lamellipodia are characterized by branched actin networks, whereas filopodia protrusions consist of long, thin, unbranched actin filaments. Lamellipodia are often described as cellular structures that drive cell migration as they are typically observed during cell migration on stiff, elastic substrates. Although filopodia have been implicated in cell–substrate adhesion and mechanosensing, their role in cell migration is not fully understood. Here, we have found that filopodia are essential for migration on soft,

viscoelastic substrates, with filopodia protrusions extending in the direction of migration and the inhibition of filopodia also blocking cell migration. The increase in filopodia length with substrate stress relaxation likely increases the probability of cell–substrate adhesion and consequently a greater traction force to support cell migration.

Computational simulations using the motor-clutch model of force transmission agree with our experimental observations and suggest additional mechanistic insights. Our 1D simulations predict that clutch lifetime increases with faster substrate relaxation, allowing cells to migrate in a given direction for a longer time. On slow-relaxing substrates, cell-substrate bonds experience a high loading rate, even at times that are well below the stress relaxation half times for the materials. Consequently, these bonds, on average, fail more quickly, resulting in a shorter lifetime. However, with sufficiently fast stress relaxation, individual bonds have a longer lifetime, resulting in a higher likelihood of formation of nascent adhesions, which consist of multiple bonds. Nascent adhesions in turn stabilize filopodia and allow them to extend much further and over longer times. However, at higher loading rates, the shorter bond lifetime results in a small filopodia lifetime, which limits how long the filopodia grows and allows cells to change migration direction more frequently. This reduces the persistence of cell migration and reduces the amount of sustained traction forces that cells can generate to support migration. Furthermore, the increased bond lifetime on fast-relaxing substrate could promote cell spreading, which leads to a greater spread area, which we observe. This finding is consistent with a previous study that demonstrated that increased integrin bond lifetime allows cells to spread on soft substrates¹⁸. Another explanation invokes the previous finding that at optimal substrate stiffness, the force loading rate on the clutch is comparable to the integrin-ECM bond lifetime²¹. This results in an increased number of engaged clutches on average and subsequently efficient traction force transmission to the substrate to drive cell migration. Higher (or lower) substrate stiffness than the optimal substrate stiffness leads to inefficient force transmission and thus impaired cell migration. In our 2D CMS simulations, the optimal migration of cells on elastic substrates is at higher stiffness. For cells on viscoelastic substrates, the optimal migration occurs at lower stiffness. For fast-relaxing substrates, the stiffness experienced by the cell decreases with time faster (Supplementary Fig. 7), potentially shifting the cell closer to the optimal stiffness and enhancing migration. Taken together, these results suggest that substrate viscoelasticity regulates bond lifetimes and/or the number of engaged clutches, which in turn mediates cell migration.

Robustly migrating cells on fast-relaxing IPNs are rounded, reminiscent of amoeboid migration⁴⁵. However, these rounded cells lack blebs, a feature of amoeboid migration, and instead display filopodia protrusions. It is probable that the rounded cell migration we observe is different from the conventional amoeboid migration observed in 3D migration models where cells are mechanically confined⁴⁵. The limited number of nascent adhesions formed does mirror the few weak adhesions observed in the migration of leukocytes, lymphocytes, dendritic cells and neutrophils on 2D substrates 10,46. However, these immune cells migrate at much greater speeds and filopodia have not been implicated in their migration, suggesting that the migration modes are distinct. Our results are contrary to previous reports that rounded, weakly adhesive cells are not detected in 2D migration models⁴⁶. Surprisingly, we have found that rounded cancer cells on soft, fast-relaxing IPNs can migrate faster on average than those cells on glass. On the whole, our findings indicate that substrate stress relaxation is an important substrate variable to be included in 2D cell migration models.

Although, the present study was conducted in two dimensions, the key findings provide a platform to further investigate the labile adhesions and filopodia extensions observed in physiologically relevant 3D environments. Specifically, the migration model described here might provide a platform to study several aspects

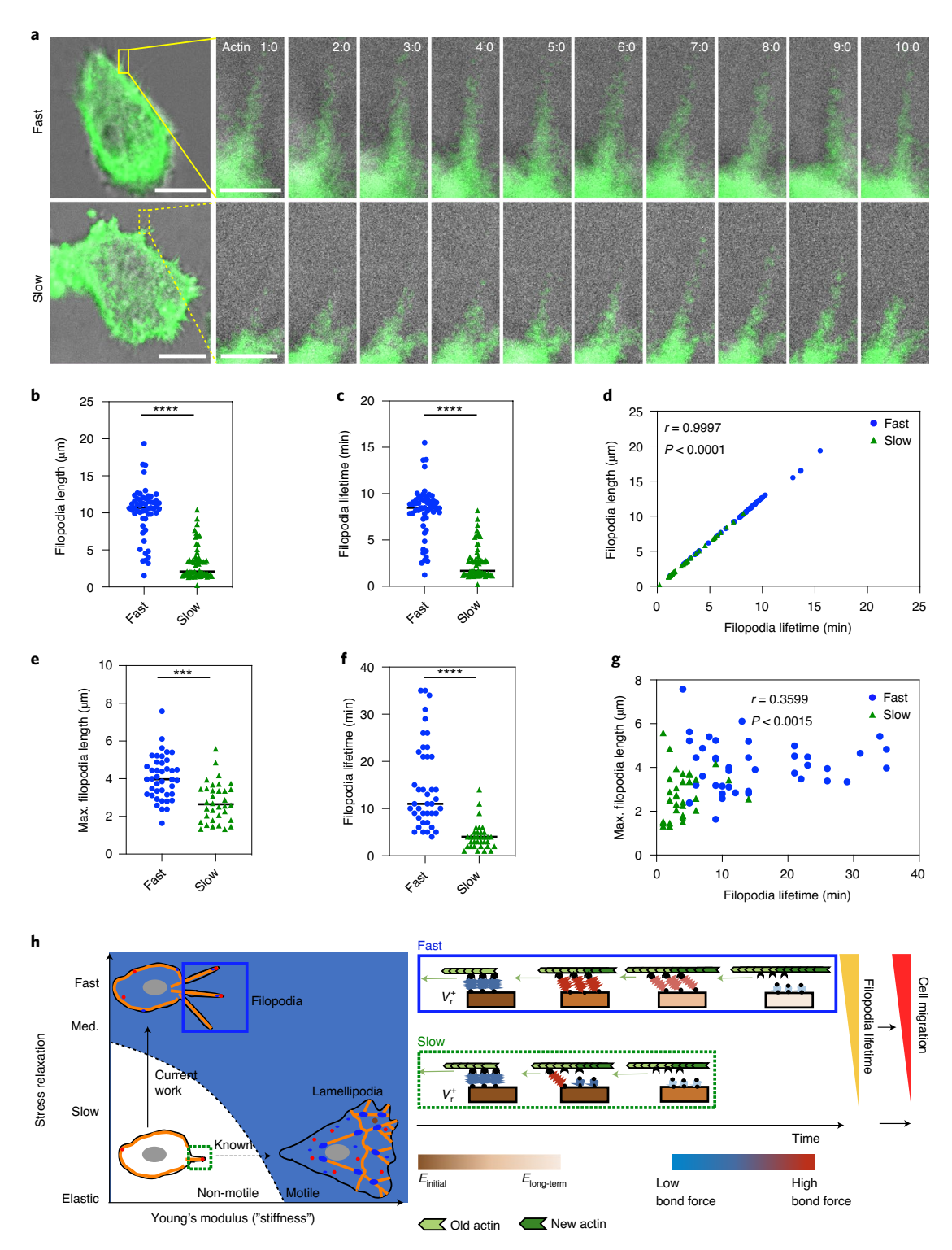


Fig. 6 | Substrate stress relaxation regulates filopodia dynamics. a, HT-1080 siR-actin-labelled cells on fast- and slow-relaxing substrates. Times are indicated in min:s. Scale bars, 10 μm; zoom-in scale bars, 5 μm. **b-d**, Motor-clutch simulations of filopodia length (**b**) and lifetime (**c**) for fast- and slow-relaxing substrates, as well as the correlation between the two parameters (**d**). The Kolmogorov-Smirnov, two-sided, test was used for data analysis, comparing with the data for the fast-relaxing hydrogel: ****P < 0.0001; n = 57 and 68 (fast and slow) cells examined over 20 independent simulations. **e-g**, Experimental quantification of filopodia length (**e**) and lifetime (**f**), as well as the correlation between the two variables (**g**), for fast- and slow-relaxing substrates with siR-actin-labelled HT-1080 cells. The Kolmogorov-Smirnov, two-sided, test was used for data analysis, comparing with the data for the fast-relaxing hydrogel for filopodia length and lifetime: ***P = 0.0006, ****P < 0.0001; n = 41 and 34 (fast and slow) cells examined over two independent samples. All statistical tests were two-sided. In **d** and **g**, r represents the Pearson correlation coefficient. The solid lines in the scatter plots indicate median values. **h**, Schematic highlighting the effect of substrate stress relaxation on cell migration in the current work. $E_{initial} > E_{long-term}$. White region, non-motile cells; blue region, motile cells. Cell-substrate bonds experience a faster loading rate on slow-relaxing substrates than on fast-relaxing substrates, resulting in a shorter lifetime and fewer bonds. The shorter bond lifetime causes less adhesion and reduced filopodia lifetime, allowing cells to change migration direction more frequently. This reduces the persistence of cell migration and impairs migration.

of cancer progression in vivo. For instance, there is strong evidence that filopodia may play a key role in cancer invasion and metastasis^{36,47}, suggesting the potential relevance of this mode of migration in vivo. In this regard, our findings have some relevance. Our results raise the possibility that, in vivo, longer filopodia facilitate the invasion of surrounding tissue¹⁹. Furthermore, the increase in filopodia number might enhance cell migration and greater exploration of the environment. In addition, in vivo evidence implicates formin and fascin, key mediators of filopodia formation, in a variety of cancers³⁶. Also, Mena, a protein implicated in filopodia formation, has oncogenic potential and contributes to chemoresistance and extravasation^{48–50}. Therefore, these results provide a fresh perspective on filopodia regulation that might be critical to cancer progression.

Online content

Any methods, additional references, Nature Research reporting summaries, source data, extended data, supplementary information, acknowledgements, peer review information; details of author contributions and competing interests; and statements of data and code availability are available at https://doi.org/10.1038/s41563-021-00981-w.

Received: 20 December 2019; Accepted: 9 March 2021; Published online: 19 April 2021

References

- Ridley, A. J. et al. Cell migration: integrating signals from front to back. Science 302, 1704–1709 (2003).
- Lauffenburger, D. A. & Horwitz, A. F. Cell migration: a physically integrated molecular process. Cell 84, 359–369 (1996).
- Shafqat-Abbasi, H. et al. An analysis toolbox to explore mesenchymal migration heterogeneity reveals adaptive switching between distinct modes. eLife 5, e11384 (2016).
- Wisdom, K. M. et al. Matrix mechanical plasticity regulates cancer cell migration through confining microenvironments. Nat. Commun. 9, 4144 (2018).
- Wolf, K. et al. Physical limits of cell migration: control by ECM space and nuclear deformation and tuning by proteolysis and traction force. *J. Cell Biol.* 201, 1069–1084 (2013).
- 6. Haston, W. S., Shields, J. M. & Wilkinson, P. C. Lymphocyte locomotion and attachment on two-dimensional surfaces and in three-dimensional matrices. *J. Cell Biol.* **92**, 747–752 (1982).
- Yamada, K. M. & Sixt, M. Mechanisms of 3D cell migration. *Nat. Rev. Mol. Cell Biol.* 20, 738–752 (2019).
- Reversat, A. et al. Cellular locomotion using environmental topography. Nature 582, 582–585 (2020).
- Hons, M. et al. Chemokines and integrins independently tune actin flow and substrate friction during intranodal migration of T cells. *Nat. Immunol.* 19, 606–616 (2018).
- 10. Friedl, P. & Wolf, K. Plasticity of cell migration: a multiscale tuning model. *J. Cell Biol.* **188**, 11–19 (2010).
- Xue, F., Janzen, D. M. & Knecht, D. A. Contribution of flopodia to cell migration: a mechanical link between protrusion and contraction. *Int J. Cell Biol.* 2010, 507821 (2010).
- Jacquemet, G., Hamidi, H. & Ivaska, J. Filopodia in cell adhesion, 3D migration and cancer cell invasion. Curr. Opin. Cell Biol. 36, 23–31 (2015).
- Jacquemet, G. et al. Filopodome mapping identifies p130Cas as a mechanosensitive regulator of filopodia stability. Curr. Biol. 29, 202–216 (2019).
- 14. Charras, G. & Sahai, E. Physical influences of the extracellular environment on cell migration. *Nat. Rev. Mol. Cell Biol.* **15**, 813–824 (2014).
- Kim, D. H. & Wirtz, D. Predicting how cells spread and migrate: focal adhesion size does matter. Cell Adh. Migr. 7, 293–296 (2013).
- Pathak, A. & Kumar, S. Independent regulation of tumor cell migration by matrix stiffness and confinement. *Proc. Natl Acad. Sci. USA* 109, 10334–10339 (2012).
- 17. Bangasser, B. L. et al. Shifting the optimal stiffness for cell migration. *Nat. Commun.* **8**, 15313 (2017).
- Oakes, P. W. et al. Lamellipodium is a myosin-independent mechanosensor. Proc. Natl Acad. Sci. USA 115, 2646–2651 (2018).
- Liou, Y. R. et al. Substrate stiffness regulates filopodial activities in lung cancer cells. PLoS ONE 9, e89767 (2014).
- Wong, S., Guo, W. H. & Wang, Y. L. Fibroblasts probe substrate rigidity with filopodia extensions before occupying an area. *Proc. Natl Acad. Sci. USA* 111, 17176–17181 (2014).

- Chan, C. E. & Odde, D. J. Traction dynamics of filopodia on compliant substrates. Science 322, 1687–1691 (2008).
- Lo, C. M., Wang, H. B., Dembo, M. & Wang, Y. L. Cell movement is guided by the rigidity of the substrate. *Biophys. J.* 79, 144–152 (2000).
- Levental, I., Georges, P. C. & Janmey, P. A. Soft biological materials and their impact on cell function. Soft Matter 3, 299–306 (2007).
- Chaudhuri, O. et al. Hydrogels with tunable stress relaxation regulate stem cell fate and activity. Nat. Mater. 15, 326–334 (2016).
- Nam, S. et al. Cell cycle progression in confining microenvironments is regulated by a growth-responsive TRPV4-PI3K/Akt-p27^{Kip1} signaling axis. Sci. Adv. 5, eaaw6171 (2019).
- Charrier, E. E., Pogoda, K., Wells, R. G. & Janmey, P. A. Control of cell morphology and differentiation by substrates with independently tunable elasticity and viscous dissipation. *Nat. Commun.* 9, 449 (2018).
- Gong, Z. et al. Matching material and cellular timescales maximizes cell spreading on viscoelastic substrates. *Proc. Natl Acad. Sci. USA* 115, E2686–E2695 (2018).
- Chaudhuri, O. et al. Extracellular matrix stiffness and composition jointly regulate the induction of malignant phenotypes in mammary epithelium. Nat. Mater. 13, 970–978 (2014).
- Chaudhuri, O. et al. Substrate stress relaxation regulates cell spreading. Nat. Commun. 6, 6364 (2015).
- Cameron, A. R., Frith, J. E. & Cooper-White, J. J. The influence of substrate creep on mesenchymal stem cell behaviour and phenotype. *Biomaterials* 32, 5979–5993 (2011).
- Nam, S. & Chaudhuri, O. Mitotic cells generate protrusive extracellular forces to divide in three-dimensional microenvironments. Nat. Phys. 14, 621–628 (2018).
- Lee, H. P., Gu, L., Mooney, D. J., Levenston, M. E. & Chaudhuri, O. Mechanical confinement regulates cartilage matrix formation by chondrocytes. *Nat. Mater.* 16, 1243–1251 (2017).
- Kelley, L. C., Lohmer, L. L., Hagedorn, E. J. & Sherwood, D. R. Traversing the basement membrane in vivo: a diversity of strategies. *J. Cell Biol.* 204, 291–302 (2014).
- Chen, M. B., Whisler, J. A., Jeon, J. S. & Kamm, R. D. Mechanisms of tumor cell extravasation in an in vitro microvascular network platform. *Integr. Biol.* 5, 1262–1271 (2013).
- Tse, J. R., & Engler, A. J. Preparation of hydrogel substrates with tunable mechanical properties. Curr. Protoc. Cell Biol. 47, 1–16 (2010).
- Arjonen, A., Kaukonen, R. & Ivaska, J. Filopodia and adhesion in cancer cell motility. Cell Adh. Migr. 5, 421–430 (2011).
- Zaidel-Bar, R., Milo, R., Kam, Z. & Geiger, B. A paxillin tyrosine phosphorylation switch regulates the assembly and form of cell-matrix adhesions. J. Cell Sci. 120, 137–148 (2007).
- Bangasser, B. L., Rosenfeld, S. S. & Odde, D. J. Determinants of maximal force transmission in a motor-clutch model of cell traction in a compliant microenvironment. *Biophys. J.* 105, 581–592 (2013).
- Heckman, C. A. & Plummer, H. K. Filopodia as sensors. *Cell Signal* 25, 2298–2311 (2013).
- Albuschies, J. & Vogel, V. The role of filopodia in the recognition of nanotopographies. Sci. Rep. 3, 1658 (2013).
- Rubiano, A. et al. Viscoelastic properties of human pancreatic tumors and in vitro constructs to mimic mechanical properties. *Acta Biomater.* 67, 331–340 (2018).
- Chaudhuri, O., Cooper-White, J., Janmey, P. A., Mooney, D. J. & Shenoy, V. B. Effects of extracellular matrix viscoelasticity on cellular behaviour. *Nature* 584, 535–546 (2020).
- 43. Nam, S. et al. Cell cycle progression in confining microenvironments is regulated by a growth-responsive TRPV4-PI3K/Akt-p27(Kip1) signaling axis. *Sci. Adv.* 5, eaaw6171 (2019).
- Sinkus, R. et al. High-resolution tensor MR elastography for breast tumour detection. *Phys. Med. Biol.* 45, 1649–1664 (2000).
- 45. Liu, Y. J. et al. Confinement and low adhesion induce fast amoeboid migration of slow mesenchymal cells. *Cell* **160**, 659–672 (2015).
- Friedl, P. & Wolf, K. Tumour-cell invasion and migration: diversity and escape mechanisms. Nat. Rev. Cancer 3, 362–374 (2003).
- Jacquemet, G. et al. L-type calcium channels regulate filopodia stability and cancer cell invasion downstream of integrin signalling. *Nat. Commun.* 7, 13297 (2016).
- Hu, K. et al. Mammalian-enabled (MENA) protein enhances oncogenic potential and cancer stem cell-like phenotype in hepatocellular carcinoma cells. FEBS Open Bio 7, 1144–1153 (2017).
- Oudin, M. J. et al. MENA confers resistance to paclitaxel in triple-negative breast cancer. Mol. Cancer Ther. 16, 143–155 (2017).
- Harney, A. S. et al. Real-time imaging reveals local, transient vascular permeability, and tumor cell intravasation stimulated by TIE2^{hi} macrophage-derived VEGFA. *Cancer Discov.* 5, 932–943 (2015).

Publisher's note Springer Nature remains neutral with regard to jurisdictional claims in published maps and institutional affiliations.

© The Author(s), under exclusive licence to Springer Nature Limited 2021

Methods

Cell culture and reagents. Human breast cancer adenocarcinoma cells MDA-MB-231 (ATCC) and human fibrosarcoma cells HT-1080 (ATCC) were cultured in high-glucose Dulbecco's modified Eagle medium (DMEM; Gibco) supplemented with 10% fetal bovine serum (Hyclone) and 1% penicillin/streptomycin (Life Technologies). MCF-10A cells obtained from ATCC were cultured in Gibco Dulbecco's Modified Eagle Medium Nutrient Mixture F-12 (DMEM/F12) 50:50 medium (Thermo Fisher) supplemented with 5% horse serum (Thermo Fisher), 20 ng ml $^{-1}$ epidermal growth factor (EGF) (Peprotech), 0.5 μ g ml $^{-1}$ hydrocortisone (Sigma), 100 ng ml $^{-1}$ cholera toxin (Sigma), 10 μ g ml $^{-1}$ insulin (Sigma) and 100 U ml $^{-1}$ penicillin/streptomycin (Life Technologies) as previously described 51 . Cells were cultured in a standard humidified incubator at 37 °C in a 5% CO $_2$ atmosphere. Cells were maintained at subconfluency and passaged every 2–3 days.

RNA interference experiments. Pooled siRNAs targeting human fascin1 and myosin-X, and a non-targeting control were obtained from Dharmacon. HT-1080 cells were transfected with DharmaFECT1 according to manufacturer instructions. Briefly, 150,000 cells were seeded into each well of a six-well plate and transfected with 10 nM siRNA in OptiMEM (Thermo Fisher). Then, 48 h post-transfection, the cells were processed for live-cell imaging or western blot analysis.

Western blotting. HT-1080 cells were lysed in 25 mM Tris pH7.4, 100 mM NaCl, 1% Triton X-100 and 1 mM EDTA with Halt Protease Inhibitor (Thermo Fisher; the concentrations were measured with a Pierce 660 nm Protein Assay Kit from Thermo Fisher), and then boiled in SDS sample buffer. Protein samples were separated by SDS-PAGE, transferred to Immobilon-FL membranes and processed with chemiluminescent horseradish peroxidase (HRP) substrate (Millipore). Raw western blot data are provided in Supplementary Fig. 8.

Hydrogel preparation. Low-molecular-weight, ultra-pure sodium alginate (Provona UP VLVG, NovaMatrix), with a molecular weight (MW) of <75 kDa, was used for fast-relaxing substrates, according to the manufacturer. Sodium alginate rich in guluronic acid blocks and with a high MW (FMC Biopolymer, Protanal LF 20/40, High-MW, 280 kDa) was used for slow-relaxing substrates. The high-MW alginate was irradiated with 8 Mrad from a cobalt source to produce medium-MW (70 kDa) alginate²⁴. Alginate was dialysed against deionized water for 3–4 days (MW cut-off of 3,500 Da), treated with activated charcoal, sterile-filtered, lyophilized and then reconstituted to 3.5 wt% in serum-free DMEM (Gibco). The use of low/medium/high-MW alginate resulted in fast/medium/slow-relaxing IPNs.

Hydrogel formation and cell seeding. For each viscoelastic gel, alginate was delivered to a $1.5\,\mathrm{ml}$ Eppendorf tube (polymer tube) and put on ice. rBM (Corning), also on ice, was added to the alginate and carefully mixed 30 times with a pipette, being careful not to generate bubbles. For experiments with fiducial marker beads, $0.2\,\mathrm{\mu m}$ fluorescent dark-red microspheres (Thermo Fisher) were added at $100\text{-}\mathrm{fold}$ dilution. Extra DMEM was added such that all substrates had a final concentration of $10\,\mathrm{mg}\,\mathrm{ml}^{-1}$ alginate and $4.4\,\mathrm{mg}\,\mathrm{ml}^{-1}$ rBM. This was mixed 30 times with a pipette. The mixture was kept on ice.

Next, different calcium sulfate concentrations were added to 1-ml Luer lock syringes (Cole-Parmer) and kept on ice to ensure that the initial Young's moduli of the fast-, medium- and slow-relaxing substrates were kept constant. The polymer mixtures were transferred to separate 1-ml Luer lock syringes (polymer syringe) and also put on ice. To generate gels, the calcium sulfate syringe was shaken to mix the calcium sulfate evenly, and was then coupled to the polymer syringe with a female-female Luer lock (Cole-Parmer), taking care not to introduce bubbles or air into the mixture. Finally, the two solutions were rapidly mixed together with 30 pumps on the syringe handles and instantly deposited into a well in an eight-well Lab-Tek dish (Thermo Scientific) that had been precoated with rBM. The Lab-Tek dish was then transferred to a 37 °C incubator and the gel was allowed to form for 1 h before cell-containing medium was added to the well.

PA gels were prepared and functionalized according to a previous method³⁵. First, 18-mm circular coverslips were cleaned with 1 N ethanol and coated with sigmacote to form a hydrophobic surface. A prepolymer solution was prepared containing acrylamide and N,N'-methylene-bis-acrylamide, and degassed for 1 h (fluorescent beads were added if used). The wells in which gels were to be deposited were activated with 3-methacryloxypropyl-trimethoxysilane for 5 min. This was done just before the prepolymer was to be mixed with crosslinking reagents. Prior to gel formation, the prepolymer solution was mixed with a 1:100 volume of 10% ammonium persulfate and a 1:1,000 volume of N,N,N',N '-tetramethylethylenediamine. Next, 80 µl of the polymer mixture was deposited on a six-well plate with a glass bottom and a cover slip was gently placed on top. When the polymerization was completed, the PA gels were carefully separated from the coverslip. The final concentrations of acrylamide and bis-acrylamide were varied to control substrate stiffness. For 2-kPa hydrogels, a 4%:0.1% ratio was used. For ~40-kPa hydrogels, the ratio was 8%:0.264%. To enable cell adhesion to the PA gel, rBM was conjugated to the gel surface using sulfosuccinimidyl 6-(4'-azido-2'-nitrophenylamino)hexanoate (sulfo-SANPAH) as protein-substrate linker.

PA gels were incubated in 1 mg ml $^{-1}$ sulfo-SANPAH in sterile water, activated with ultraviolet light (wavelength 365 nm, intensity 15 W) for 3.5 min, washed in calcium containing Dulbecco's Phosphate Buffered Saline (cDPBS) and then incubated in 0.2 mg ml $^{-1}$ rBM in cDPBS overnight. Excess protein was washed off with cPBS before use. All hydrogel formulations are detailed in Supplementary Table 1.

For the 2D migration assays, the cells were washed with PBS, trypsinized using 0.05% trypsin/EDTA, resuspended in growth medium containing octadecyl rhodamine B chloride (R18, Thermo Fisher, 1:1,000 dilution of $10\,\mathrm{mg\,m^{1-1}}$ stock solution), centrifuged and resuspended in growth medium. The concentration of cells was determined using a Vi-Cell Coulter counter (Beckman Coulter) after passing through a 40 μ M filter (Thermo Fisher) to obtain single-cell suspensions. Cells were seeded onto the gels 1h after the gels were made. The final concentration of cells was 4,500 cells cm⁻² in each well.

Mechanical characterization of IPNs. Rheology experiments were carried out with a stress-controlled AR2000EX rheometer (TA Instruments). The IPNs for rheology testing were deposited directly onto the bottom Peltier plate. A 25-mm flat plate was then slowly lowered to contact the gel, forming a 25-mm disk gel. Mineral oil (Sigma) was applied to the edges of the gel to prevent dehydration. To measure the modulus, a time sweep was performed at 1 rad s⁻¹, 37 °C and 1% strain for 3 h, after which the storage and loss moduli had equilibrated. Young's modulus (E) was calculated, assuming a Poisson's ratio (ν) of 0.5, from the equation:

$$E = 2(1+\nu)G^*, (1)$$

where the complex modulus (G^*) was calculated from the measured storage (G') and loss moduli (G'') using:

$$G^* = (G'^2 + G''^2)^{1/2}. (2)$$

For the stress relaxation experiments, after the time sweep, a constant strain of 5% was applied to the gel at 37 °C, and the resulting stress was recorded over the course of 3 h. For the plasticity measurements, the time sweep was followed by a creep-recovery test in which a stress of $100\,\mathrm{Pa}$ was applied to the gel and the resulting strain was measured over the course of 1 h. The sample was then unloaded ($0\,\mathrm{Pa}$) and the strain was measured over an additional 2 h. The stress relaxation and creep-recovery results established that the gels behaved as viscoelastic solids.

Immunofluorescence for fixed cells. For the immunofluorescence analysis, cells were seeded on gels as previously described. After 24 h, the media were removed from the gels. Three drops of low-melting-temperature agarose were added to each well to prevent gel floating in the subsequent steps. The gels were washed once with serum-free DMEM and then fixed with 4% paraformaldehyde in serum-free DMEM, at room temperature, for 20 min. The gels were then washed, three times, with cPBS for 10 min each time. After this, the cells were permeabilized with a permeabilizing solution for 15 min and washed twice with cPBS, 5 min each time. Blocking solution was then added to minimize non-specific staining. The final steps were addition of the primary antibody overnight at room temperature, washing twice with cPBS, addition of the secondary antibody at room temperature for 1.5h and a final wash with cPBS. ProLong Gold antifade reagent (Life Technologies) was added just before imaging to minimize photobleaching. Images were acquired with a Leica ×25 objective.

The following primary antibodies were used: anti-paxillin antibody Y113 (1:500, Abcam ab32084), anti-focal adhesion kinase (1:500, Thermo Fisher 700255), anti-myosin light chain, phosphor-specific S19 (1:250, EMD Millipore AB3381), anti-myosin-X (1:250, Novus Biologicals 22430002) and anti-VASP (1:100, Origene TA502647). Matching secondary antibodies purchased from Life Technologies were used. Alexa Fluor 488 phallodin was used to label actin (1:80, Life Technologies), and DAPI was used to label the nuclei (1:500, Sigma).

Confocal microscopy. All microscope imaging was performed with a laser scanning confocal microscope (Leica SP8) fitted with a temperature/incubator control suitable for live imaging (37°C, 5% CO₂). In live-cell time-lapse imaging, R18 membrane-labelled cells were tracked with a ×10 numerical aperture (NA) = 0.4 air objective for 24 h. A \times 25 NA = 0.95 water-matched objective was used for experiments with fluorescent beads, immunofluorescence imaging and for siR-actin-labelled cell experiments for filopodia analysis. For live-cell time-lapse imaging, 60-µm stack images were acquired every 10 min, and imaging parameters were adjusted to minimize photobleaching and avoid cell death. For siR-actin imaging for filopodia analysis, 15-µm stack images were acquired every 1 min after it was determined that this imaging frequency did not cause cell death. Gels were inverted to obtain high-resolution filopodia and lamellipodia images. Briefly, HT-1080 cells were seeded on fast- and slow-relaxing gels and allowed to spread overnight in a four-well Lab-Tek chamber (Thermo Scientific) with removable wells. The cells were then fixed with 4% paraformaldehyde and incubated with siR-actin for 5 h. Next, the Lab-Tek wells were removed and a rectangular coverslip was gently placed over the gel. The assembly was flipped, and the cells were imaged through the coverslip using a $\times 25$ NA = 0.95 water-immersion objective.

Morphometric and traction stress analysis. To quantify cell circularity and cell area, the confocal images of R18-labelled cells were analysed in ImageJ (https://imagej.nih.gov/ij/) to calculate circularity and cell area. Circularity, mathematically calculated as $4\pi\times area\times (perimeter)^{-2}$, ranges from 0 to 1 with a value of 1 being a perfect circle. For the speed versus circularity plots, randomly selected cells were manually tracked. The corresponding instantaneous speed and circularity were determined using the default algorithm of ImageJ. In cell migration simulations, the cell aspect ratio is defined as the ratio of the longest axis to the shortest axis, and cell area is determined as the area of the ellipse that best fits the cross-section of the cell.

For matrix displacement analysis, the bead displacement obtained from confocal imaging was converted into matrix displacement fields following established protocols 4,52 . Briefly, isolated, single cells that produced observable bead displacement were used for the analysis. Cell and bead channel images, from a single z plane, were corrected for drift using the StackReg ImageJ plugin. Next, the particle image velocimetry (PIV) ImageJ plugin was used to perform a PIV analysis on the bead data. The PIV algorithm maximizes the cross-correlation between relaxed and strained images. A two-pass PIV with 128×64 pixel size was used on all images for the PIV analysis. The resulting analysis produced the position and vector field of the bead displacement. Custom MATLAB code was used to visualize the vector fields and heat maps.

Imaris cell tracking algorithm. For the migration studies, the centroids of R18-labelled cells were tracked using the spot detection functionality in Imaris (Bitplane). Poorly segmented cells and cell debris were excluded from the analysis and drift correction was implemented where appropriate. A custom MATLAB script was used to reconstruct the cell migration trajectory.

Inhibition studies. Pharmacological inhibitors were added to cell media 10 min before time-lapse microscopy experiments. The concentrations used for the inhibitors were 100 nM latrunculin A (Tocris Bioscience, actin polymerization inhibitor), 70 μ M NSC 23766 (Tocris Bioscience, Rac1 inhibitor), 50 μ M CK 666 (Sigma, Arp2/3 inhibitor), 20 μ M ML141 (Tocris, Cdc42 GTPase inhibitor), 20 μ M SMIFH2 (Sigma, formin inhibitor), 30 μ M fascin-G2 (Xcess Biosciences, fascin inhibitor), 50 μ M Y-27632 (Sigma, ROCK inhibitor), 25 μ M ML-7 (Tocris, myosin light-chain kinase inhibitor), 2 μ g ml $^{-1}$ CD29 monoclonal antibody TS2/16 (Life Technologies, β l-integrin activator) and 5 μ g ml $^{-1}$ monoclonal β l-integrin-blocking antibody (Abcam, P5D2). For the HT-1080 cell detachment studies, the cells were seeded on fast- and slow-relaxing gels and allowed to spread overnight. Then, $10\,\mu$ g ml $^{-1}$ monoclonal β l-integrin-blocking antibody was added to the media and live-cell imaging started. Images were acquired every 2 min for 12 h.

Calcium imaging. To quantify the relative level of intracellular calcium depending on the substrate type, ratiometric calcium imaging was performed with two intracellular calcium indicators, namely Fluo-3 AM (20 μ M, Thermo Fisher) and Fura-red AM (33 μ M, Thermo Fisher) 53 . HT-1080 cells were incubated in both dyes for 1 h and washed twice with DPBS. Live-cell confocal microscopy was used to measure the intensity of calcium indicators in the cells. Both calcium indicators were excited at 488 nm and detected at 515–580 nm (Fluo-3) and >610 nm (Fura-red) to measure the fluorescent intensities. The relative level of intracellular calcium was measured as the intensity ratio of Fluo-3 to Fura-red.

Statistics and reproducibility. All measurements were performed on 1–3 biological replicates from separate experiments. The exact sample size and exact statistical test performed for each experiment are indicated in the appropriate figure legends. Statistical analyses were performed using GraphPad Prism (GraphPad Prism version 9.1.0 for Mac laptop, GraphPad Software, http://www.graphpad.com). For all violin plots, the dashed lines represent median values. For scatter plots, the solid lines indicate median values. The reported *P* values were corrected for multiple comparisons, where appropriate. Additional information on the statistical tests is provided in Supplementary Table 2. All immunofluorescence and live-actin experiments were performed over three independent experiments.

Cell migration simulation based on the motor-clutch framework. The primary components of the mechanosensing apparatus in cells are actin-myosin (motor) and cell-ECM adhesion (clutch), also known as the motor-clutch module, the dynamics of which have successfully explained the stiffness sensing of cells on elastic substrates^{17,21}. In the motor-clutch module, myosin motors pull F-actin towards the cell centre and form an actin retrograde flow. This retrograde flow is resisted by adhesion molecules, which can randomly bind and unbind between actin bundles and the ECM. At the cell leading edge, the polymerization of actin filaments, countered by retrograde flow, pushes the cell membrane forward, resulting in the protrusion of the cell. To account for the viscoelasticity of the ECM, an SLS model containing three elements, namely long-term modulus, additional modulus and viscosity, is applied. For a cell to migrate, the symmetry or velocity balance between the cell's ends has to be broken by the stochastic dynamics of the clutches. Hence, two or more motor-clutch modules can be connected, and their forces are balanced at the cell centre.

We first applied the 2D CMS, which is composed of multiple motor-clutch modules, to investigate cell migration differences on soft, fast- and slow-relaxing viscoelastic substrates as well as on soft and stiff elastic substrates (Supplementary Notes). To further study the symmetry breaking associated with cell migration and gain mechanistic insights, we simplified this set-up to create a 1D model with two connected motor-clutch modules (Supplementary Notes). The dynamics of each motor-clutch module can also be used to characterize filopodia dynamics²¹. Filopodia lifetime is defined as the time that elapses from the initial attachment of clutches to the catastrophic breakage of the entire clutch cluster leading to filopodia retraction. Simulation parameters are provided in Supplementary Tables 3 and 4. CMS simulations were carried out with custom C++ code, and 1D simulations were carried out in MATLAB. Details of the formulations and algorithms used can be found in the Supplementary Notes.

Reporting Summary. Further information on research design is available in the Nature Research Reporting Summary linked to this article.

Data availability

All data relevant to this manuscript are available upon request. Source data are provided with this paper.

Code availability

All analyses codes relevant to this manuscript have been deposited in the DOI-minting repository Zenodo⁵⁴. Simulation codes are available upon request.

References

- Lee, J. Y. et al. YAP-independent mechanotransduction drives breast cancer progression. *Nat. Commun.* 10, 1848 (2019).
- 52. Poincloux, R. et al. Contractility of the cell rear drives invasion of breast tumor cells in 3D matrigel. *Proc. Natl Acad. Sci. USA* 108, 1943–1948 (2011).
- Lee, H. P., Stowers, R. & Chaudhuri, O. Volume expansion and TRPV4 activation regulate stem cell fate in three-dimensional microenvironments. *Nat. Commun.* 10, 529 (2019).
- Adebowale, K. et al. Enhanced substrate stress relaxation promotes filopodia-mediated cell migration. Zenodo https://doi.org/10.5281/ zenodo.4562343 (2021).

Acknowledgements

We acknowledge R. Stowers (University of California, Santa Barbara) and the Chaudhuri laboratory for helpful discussion, and M. Levenston (Stanford University) for use of mechanical testing equipment. We also acknowledge the Stanford Cell Sciences Imaging Facility for Imaris software access and for technical assistance with Imaris. Figure 5n is a schematic created with BioRender.com. K.A. acknowledges financial support from the Stanford ChEM-H Chemistry/Biology Interface Predoctoral Training Program and the National Institute of General Medical Sciences of the National Institutes of Health under Award Number T32GM120007, and a National Science Foundation (NSF) Graduate Student fellowship, D.G. was funded in part by a National Institutes of Health Fellowship under Award Number GM116328. This work was supported by a National Institutes of Health National Cancer Institute (NIH NCI) grant (U54 CA210190) for D.J.O. and NIH NCI grant R01 CA232256, NIH National Institute of Biomedical Imaging and Bioengineering awards R01EB017753 and R01EB030876, NSF Center for Engineering Mechanobiology grant CMMI-154857, and NSF grants MRSEC/DMR-1720530 and DMS-1953572 to V.B.S., and by an American Cancer Society grant (RSG-16-208-01) and a NIH NCI grant (R37 CA214136) to O.C.

Author contributions

K.A. and O.C. designed the experiments. K.M.W. designed the material system. K.A. performed rheometry, substrate preparation, time-lapse microscopy cell migration, immunofluorescence and filopodia experiments. H.L. performed the calcium imaging experiments. S.N. helped with the traction force experiments. D.G. and T.M. performed the siRNA knockdown experiments. K.A. performed all experimental data analysis and statistical tests. Z.G., V.B.S., J.C.H. and D.J.O. performed the computer simulations and analysis. K.A., Z.G., J.C.H., V.B.S., D.J.O. and O.C. wrote the manuscript.

Competing interests

The authors declare no competing interests.

Additional information

 $\label{thm:contains} \textbf{Supplementary information} \ The online version contains supplementary material available at $$https://doi.org/10.1038/s41563-021-00981-w.$

Correspondence and requests for materials should be addressed to O.C.

Reprints and permissions information is available at www.nature.com/reprints.

Peer review Information Nature Materials thanks Pakorn Kanchanawong and the other, anonymous, reviewer(s) for their contribution to the peer review of this work.



Corresponding author(s):	Ovijit Chaudhuri
Last updated by author(s):	Feb 10, 2021

Reporting Summary

Nature Research wishes to improve the reproducibility of the work that we publish. This form provides structure for consistency and transparency in reporting. For further information on Nature Research policies, see <u>Authors & Referees</u> and the <u>Editorial Policy Checklist</u>.

_				
7	ta	tι	ςt	ics

For	all statistical analys	ses, confirm that the following items are present in the figure legend, table legend, main text, or Methods section.			
n/a	Confirmed				
	The exact sar	nple size (n) for each experimental group/condition, given as a discrete number and unit of measurement			
	A statement	on whether measurements were taken from distinct samples or whether the same sample was measured repeatedly			
	The statistical test(s) used AND whether they are one- or two-sided Only common tests should be described solely by name; describe more complex techniques in the Methods section.				
\boxtimes	A description	of all covariates tested			
	A description	of any assumptions or corrections, such as tests of normality and adjustment for multiple comparisons			
	A full description of the statistical parameters including central tendency (e.g. means) or other basic estimates (e.g. regression coefficient AND variation (e.g. standard deviation) or associated estimates of uncertainty (e.g. confidence intervals)				
	For null hypothesis testing, the test statistic (e.g. <i>F</i> , <i>t</i> , <i>r</i>) with confidence intervals, effect sizes, degrees of freedom and <i>P</i> value noted Give <i>P</i> values as exact values whenever suitable.				
\boxtimes	For Bayesian analysis, information on the choice of priors and Markov chain Monte Carlo settings				
\boxtimes	For hierarchical and complex designs, identification of the appropriate level for tests and full reporting of outcomes				
\square Estimates of effect sizes (e.g. Cohen's d , Pearson's r), indicating how they were calculated					
		Our web collection on <u>statistics for biologists</u> contains articles on many of the points above.			
Software and code					
Poli	cy information abo	ut <u>availability of computer code</u>			
D	ata collection	Leica SP8 (Leica confocal microscopy images). TA instruments (acquisition of rheometry data).			
D	ata analysis	1. Graphpad PRISM 8 (used for plotting all graphs, and statistical analysis). 2. Imaris (used for cell tracking). 3. Matlab (used for analyzing raw data before plotting in PRISM). 4. ImageJ (used for displaying immunohistochemistry staining images). 5. Adobe Illustrator (used for figure preparation). 6. Microsoft Excel (data handling).			

For manuscripts utilizing custom algorithms or software that are central to the research but not yet described in published literature, software must be made available to editors/reviewers. We strongly encourage code deposition in a community repository (e.g. GitHub). See the Nature Research guidelines for submitting code & software for further information.

Data

Policy information about availability of data

All manuscripts must include a <u>data availability statement</u>. This statement should provide the following information, where applicable:

- Accession codes, unique identifiers, or web links for publicly available datasets
- A list of figures that have associated raw data
- A description of any restrictions on data availability

Data supporting findings in this manuscript are available upon reasonable request from the corresponding author.

Field-spe	cific reporting			
Please select the o	ne below that is the best fit for your research. If you are not sure, read the appropriate sections before making your selection.			
X Life sciences	Behavioural & social sciences Ecological, evolutionary & environmental sciences			
For a reference copy of	he document with all sections, see <u>nature.com/documents/nr-reporting-summary-flat.pdf</u>			
Life scier	nces study design			
All studies must dis	close on these points even when the disclosure is negative.			
Sample size	Sample size was determined by following the range of sample sizes from previous studies relevant to our work used. These provided sufficient power for statistical analyses. This gave us confidence in the statistical power of our analyses. (Refs: Wisdom doi: 10.1038/s41467-018-06641-z, Loebel doi: 10.1038/s41563-019-0307-6 Lee doi: 10.1038/s41467-019-08465-x).			
Data exclusions	No data was excluded from the experiments.			
Replication	All experiments were replicated from distinct samples and independent experiments performed on separate days. Great care was taken to minimize experimenter error.			
Randomization	Materials used for making hydrogels were prepared from different batches. Hydrogels were deposited in wells in a randomized fashion. For imaging, multiple fields of view were randomly selected.			
Blinding	Blinding was not relevant to the current work since the metrics are quantified and objectively analyzed.			
Reporting for specific materials, systems and methods				
	on from authors about some types of materials, experimental systems and methods used in many studies. Here, indicate whether each material, led is relevant to your study. If you are not sure if a list item applies to your research, read the appropriate section before selecting a response.			
Materials & ex	perimental systems Methods			
n/a Involved in th	e study n/a Involved in the study			
Antibodies	ChIP-seq			
Eukaryotic				
Palaeontol	ogy MRI-based neuroimaging			
	d other organisms			
Human research participants				
Clinical dat	a a control of the co			
Antibodies				
Antibodies used	Antibodies used have been explicitly described in the Methods section of the manuscript.			
Validation	All antibodies were newly purchased from manufacturers and came with a warranty and validation paperwork.			
Eukaryotic c	ell lines			
Policy information	about <u>cell lines</u>			
Cell line source(s	HT-1080 and MDA-MB-231 cells were purchased from ATCC.			

Cell lines were authenticated from manufacturer (ATCC).

No commonly misidentified cell lines were used.

Not performed.

Authentication

(See <u>ICLAC</u> register)

Mycoplasma contamination

Commonly misidentified lines